

SCIENTIFIC REPORTS



OPEN

Compact wideband plasmonic filter with flat-top transmission response based on corrugated metal-insulator-metal ring resonator

Liu Yang, Yong Jin Zhou, Chao Zhang & Qian Xun Xiao

We demonstrate a novel route to control the filtering of spoof localized surface plasmons (LSPs) on the corrugated metal-insulator-metal (MIM) ring resonator. The spoof LSPs resonance modes can be effectively tuned to achieve broad passband (covering the quadrupole mode and the hexapole mode) by selecting proper lengths in the input and output coupling area. The mutual coupling between the input and output lines produces the flat-top transmission response and sharp out-of-band rejection. Compared with the wideband bandpass filters based on spoof plasmonic waveguides, the proposed filter is ultra-compact and only $0.35\lambda \times 0.35\lambda$. In order to further improve the property of the bandpass plasmonic filter, all the out-of-band frequencies (the dipole mode and the octopole mode) have been rejected by introducing a shunt stepped-impedance resonator and double C-shaped rings on the back of the substrate of the filter. Simulated results are confirmed via experiment, showing good rejection and wideband filtering performance with low insertion loss, flat-top transmission response and sharp out-of-band suppression. The proposed filter can find more applications in the highly integrated plasmonic circuits and systems in both terahertz and microwave regimes.

Surface plasmons (SPs) have attracted enormous research attention in recent years, due to their capabilities of breaking the classical diffraction limit and manipulating light at the sub-wavelength scale¹. SPs exist either as propagating surface plasmon polaritons (SPPs) on the extended interface between metal and dielectric or localized surface plasmons (LSPs) on finite metal particles². The study of generating and manipulating SPs has been expanded from the optical regime to microwave and terahertz (THz) regime, thanks to the pioneering work from Pendry *et al.*³. These surface modes on the structured metal surface are widely termed as designer or spoof SPs. These spoof plasmonic structures possess not only similar capacity of field confinement and non-diffraction limit as that of optical SPs, but also the flexible controllability by tailoring the geometrical parameters on patterns due to their millimeter scale size. While most of these studies focused on propagating spoof SPPs⁴⁻⁶, recently, spoof LSPs have been demonstrated using spoof plasmonic resonators⁷⁻¹⁰.

Spoof SPPs waveguides are often used to design wideband bandpass filter¹¹⁻¹⁵. Among the various plasmonic waveguides, the metal-insulator-metal (MIM) waveguides allow the highly confined SPPs modes to propagate in a sharp bend with low additional transmission loss and a simple fabrication technique¹⁶. Spoof plasmonic analogue of MIM waveguides was then proposed¹⁷ and ultra-wideband bandpass filters based on spoof MIM waveguides have been studied at microwave frequencies¹⁸⁻²⁰. However, efficient conversions between spoof SPPs and guided waves are necessary for feeding energies into and extracting signals from functional plasmonic devices through transmission lines. Hence, the length of these wideband filters in the propagation direction is typically several wavelengths. Although LSPs resonators are compact, they are usually used to implement narrowband filters with asymmetrical teeth-shaped structure²¹, MIM nanodisk cavity²², corrugated ring resonator²³, etc. Besides, by controlling the couplings between the spoof LSPs particles and the spoof SPPs waveguides^{24,25}, narrowband rejection filters have been proposed. To broaden the operating band, different structures such as a symmetrical multiple-teeth-shaped structure²⁶, a metal bar loaded into the stub²⁷, a graded plasmonic resonator chain²⁸, an ultra-thin periodic corrugated metallic strip with defect units²⁹ and so on, have been investigated. However, such methods will not only increase the filter length, but also bring in additional transmission loss. Moreover, most of

Key Laboratory of Specialty Fiber Optics and Optical Access Networks, Shanghai University, Shanghai, 200444, China. Correspondence and requests for materials should be addressed to Y.J.Z. (email: yjzhou@shu.edu.cn)

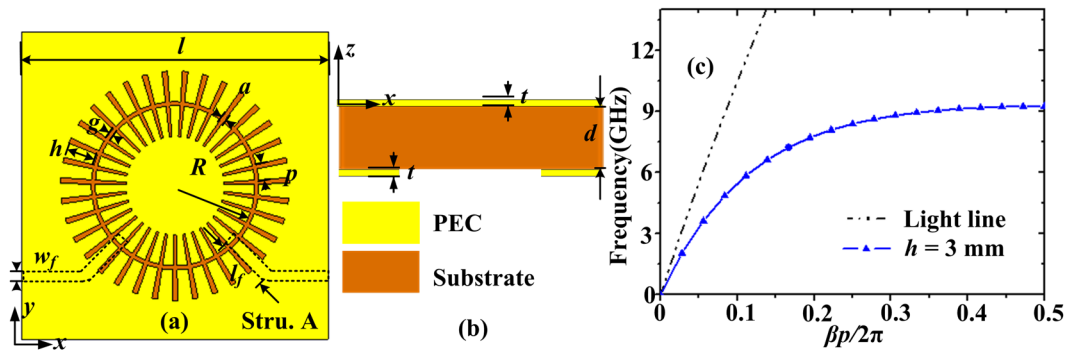


Figure 1. (a) The top view and (b) the side view of the schematic diagram of the narrowband bandpass filter (structure A) composed of grooved MIM ring resonator and the input and output microstrip lines, where the parameters l , h and g of the MIM ring are 30 mm, 3 mm and 0.4 mm, the metal thickness t and the substrate thickness d are 18 μm and 0.635 mm, and w_f and l_f of the microstrip line are 0.64 mm and 5 mm, respectively. (c) Dispersion curve of spoof SPPs on the corrugated MIM strips when the groove depth h is 3 mm.

plasmonic filters mentioned above have a Lorentzian-shaped transmission response, not the flat-top transmission response which is required for many communication systems. Squared ring resonators³⁰ and cascaded rectangular ring resonators³¹ have been designed as bandpass filters with flat-top transmission response. To the best of our knowledge, there is no reported work on plasmonic wideband bandpass filter with flat-top transmission response based on spoof LSPs resonators.

The corrugated MIM ring resonator has been fully investigated in Ref.³². In this paper, an ultra-compact and wideband bandpass plasmonic filter based on the corrugated MIM ring resonator has been numerically and experimentally demonstrated. Different from almost all of the above filters, where their resonance wavelengths are often changed by modifying the geometrical parameters of the resonators, a new adjusting mechanism is applied to broaden the transmission band covering the quadrupole mode and the hexapole mode. It has been shown that the spoof LSPs resonance modes can be effectively tuned by selecting proper lengths in the input and output coupling area. By introducing the mutual coupling between the input and output lines, flat-top transmission and sharper out-of-band rejection can be achieved. The whole wideband bandpass filter is only $0.35\lambda \times 0.35\lambda$ and ultra-compact, compared with the previously mentioned wideband bandpass filters based on spoof SPPs waveguides. In order to further improve the property of the bandpass filter, some other methods are used to reject all the frequencies outside the interested passband. By introducing a shunt stepped-impedance resonator (SIR) and double C-shaped rings on the back of the substrate of the filter, the rejections of the dipole mode and the octopole mode have been implemented. Hence, the spoof plasmonic filter exhibits several attractive features such as ultra-compact size, wide bandwidth, low insertion loss, flat-top transmission response and sharp out-of-band suppression. The measured results agree well with the simulated results. The structures can find more applications in the highly integrated plasmonic circuits and systems at microwave and THz frequencies.

Results and Discussion

Design of wideband filtering of spoof LSPs. The corrugated MIM ring resonator is composed of two closed corrugated metal strips printed on the substrate Rogers RO3010 whose thickness d is 0.635 mm, as illustrated in Fig. 1(a) and (b). The side length l of the structure is 30 mm. The metal thickness t is 18 μm . The number N of the grooves is 35 and the groove depth h is chosen as 3 mm. Both the groove period and groove width of the corrugated MIM ring resonator (on the plane $z=0$) are non-uniform. The groove period is determined by $2\pi R/N$ and the groove width is $2\pi R * 2.8/360$, where R is the local radius of the ring. For simplicity, the insulator of the MIM ring is set to air and its inner radius is set as 7.8 mm. The width g of the air is 0.4 mm. The dispersion characteristics have been calculated and shown in Fig. 1(c), where the mean groove width and groove period are used and they are 0.40 mm and 1.47 mm, respectively. It has been verified that the spoof LSPs are actually standing waves and they satisfy the relation $L \approx n \cdot \lambda_g$, where L is the circumference of the air ring, λ_g is the guided wavelength on the corrugated MIM resonator and n is the mode number³².

In ref.³², it has been shown that spoof LSPs modes in the corrugated MIM ring can be efficiently excited by use of a microstrip line and the exciting efficiency depends on the matching degree between the magnetic field of the exciting source and that in the corrugated MIM ring. Here, by adding an output microstrip line which is perpendicular to the input microstrip feed line (see the dashed lines in Fig. 1(a)), a narrowband bandpass filter denoted as structure A can be implemented. The width w_f and length l_f of the 50 Ω microstrip line are 0.64 mm and 5 mm, respectively. The reflection and transmission coefficients of the filter are obtained and given in Fig. 2(a). The resonance modes are marked as m_1 - m_4 , whose resonance frequencies are 2.0 GHz, 3.51 GHz, 4.87 GHz, and 5.83 GHz, respectively. To understand the operating mechanisms, the two-dimensional (2D) E_z -field distributions on the xoy plane 1 mm above the structure at these resonant frequencies are illustrated in Fig. 2(b). It can be seen that the dipole ($n=1$), quadrupole ($n=2$), hexapole ($n=3$) and octopole ($n=4$) modes have been effectively excited. Since the electric fields are very weak at the output coupling area for the dipole mode and the hexapole mode, it's expected that the two odd modes would not be coupled out. From the transmission coefficients in Fig. 2(a), we can see that the odd order modes are suppressed due to the configuration of the output and input microstrip lines, while the even order modes can be coupled out. However, their transmission bandwidths are very narrow. The

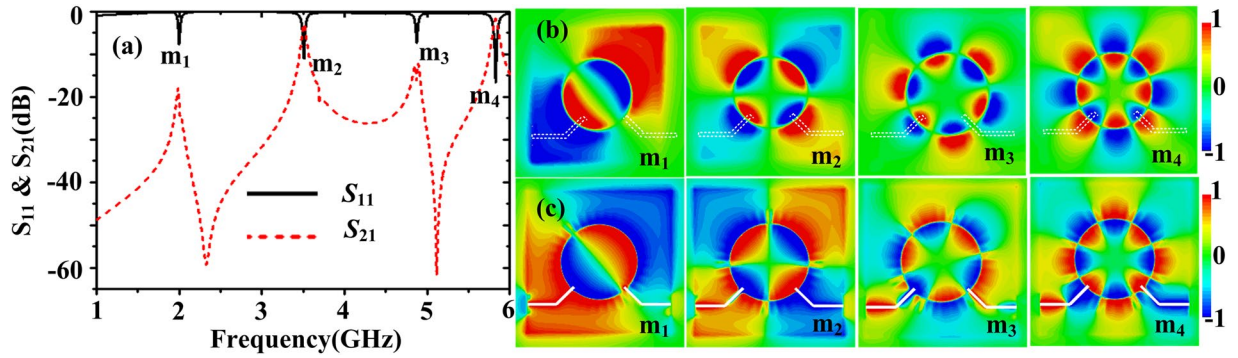


Figure 2. (a) Reflection and transmission coefficients of the spoof plasmonic narrowband bandpass filter (structure A). 2D E_z -field distributions on the plane (b) $z = 1$ mm and (c) $z = -0.635$ mm of the narrowband bandpass filter (structure A).

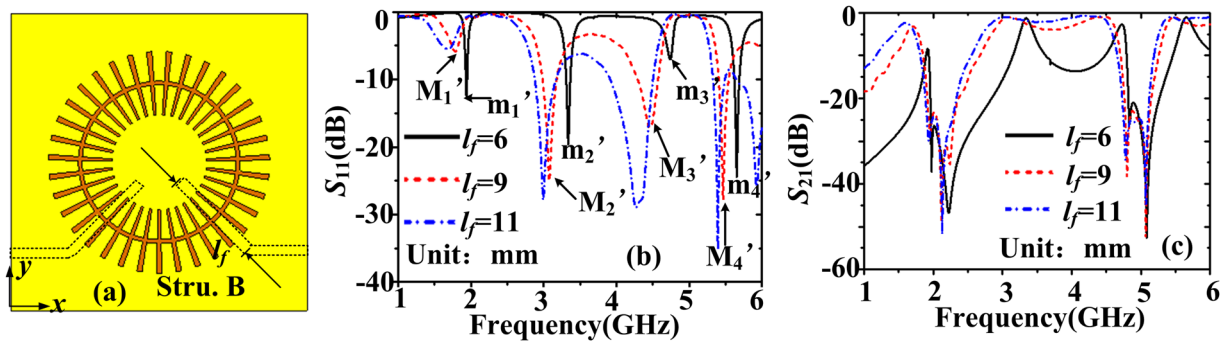


Figure 3. (a) The top view of the wideband bandpass filter with $l_f = 9$ mm (structure B). (b) Reflection coefficients and (c) transmission coefficients of the wideband bandpass filter when l_f changes from 6 mm to 11 mm.

full width at half maximum (FWHM) is 10 MHz for m_2 mode and it is 40 MHz for m_4 mode. The insert losses are -2.99 dB and -1.8 dB, respectively. Furthermore, the transmission response is Lorentzian-shaped. Figure 2(c) illustrates the 2D E_z -field distributions on the plane $z = -0.635$ mm (the bottom of the filter structure) at these resonant frequencies. We can see that the field distributions on the plane $z = -0.635$ mm are the same as those on the plane $z = 1$ mm.

Next, we will investigate how and why the operating passband can be broadened. When the feeding microstrip is extended approximately one-quarter wavelength beyond the point of crossing, a broadband transition can be achieved³³. The operating central frequency of the wideband filter is set to 3.5 GHz. Hence, the objective is to efficiently excite the quadrupole ($n = 2$) mode and the hexapole ($n = 3$) mode simultaneously, whose corresponding guided wavelengths are about 24.5 mm and 16.3 mm, respectively. When l_f is increased to 9 mm, the filter is denoted as structure B, shown in Fig. 3(a). When the length l_f of the input and output microstrip lines changes, the simulated quadrupole mode and the hexapole mode in Fig. 3(b). The new resonance modes are marked as m_1' – m_4' and M_1' – M_4' for $l_f = 6$ mm and $l_f = 9$ mm. The resonance frequencies are 1.94 GHz, 3.34 GHz, 4.74 GHz, and 5.66 GHz for m_1' – m_4' modes. For M_1' – M_4' modes, they are 1.77 GHz, 3.06 GHz, 4.43 GHz, and 5.41 GHz, respectively. First, we can see that the reflected waves have been decreased below -5 dB in the band between the M_2' mode and M_3' mode. The transmission spectra are plotted in Fig. 3(c). There exist two narrow bands (corresponding to the quadrupole mode and the hexapole mode) from 2.5 GHz to 5 GHz when $l_f = 6$ mm. When l_f is increased to 9 mm, we can see that the transmission band expands and its FWHM becomes 1.64 GHz. At this time, the extended length of the input line beyond the point of crossing is about 4.5 mm which is between one-quarter wavelengths of the quadrupole mode and the hexapole mode (4.075 mm–6.125 mm). That is, the length of the input microstrip line is set to be approximate a quarter wavelength of the chosen central frequency (3.5 GHz). Hence, a wideband passband covering the excited two resonant modes can be formed. Second, it can be seen that the resonance frequencies red shift when l_f is increased. Because the extended lengths of the input line beyond the point of crossing are still in the range of one-quarter wavelengths of the quadrupole mode and the hexapole mode (4.075 mm–6.125 mm) when l_f is larger than 9 mm and no larger than 11 mm, broad passband (covering the quadrupole mode and the hexapole mode) can also be achieved. However, The FWHM is almost unchanged when l_f is larger than 9 mm. For example, the FWHM is 1.67 GHz when l_f is 11 mm which is almost the same as that for $l_f = 9$ mm. While the input and output microstrip lines are very close when $l_f = 11$ mm. Hence, the final length l_f is set to 9 mm. To reveal the physical mechanisms, Fig. 4(a) and (b) illustrate the simulated E_z -field distributions for the m_1' – m_4' modes on the plane $z = 1$ mm and $z = -0.635$ mm, respectively. We can see that the electric field

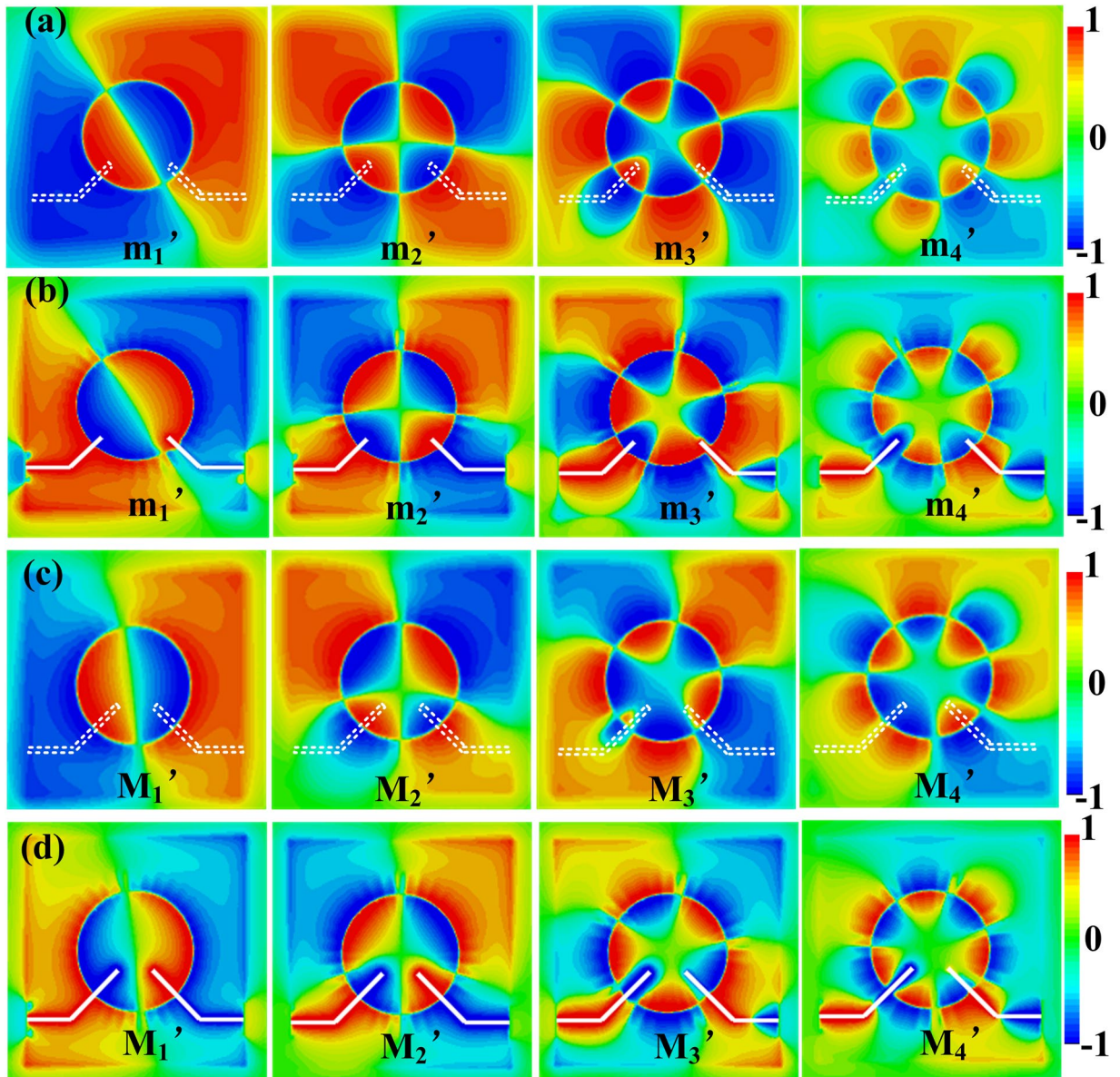


Figure 4. 2D E_z -field distributions (a) on the plane $z = 1$ mm and (b) on the plane $z = -0.635$ mm when $l_f = 6$ mm. 2D E_z -field distributions (c) on the plane $z = 1$ mm and (d) on the plane $z = -0.635$ mm when $l_f = 9$ mm.

distributions on the plane $z = 1$ mm are almost the same as those on the plane $z = -0.635$ mm except for the m_4' mode. From Fig. 4(b), we can see that the input coupling line constitutes one pole of the octopole mode for the m_4' mode, while it is not obvious for the m_3' mode. Figures 4(c) and (d) illustrate the simulated E_z -field distributions for the M_1' – M_4' modes on the plane $z = 1$ mm and $z = -0.635$ mm, respectively. With further increase of l_f , we can see that the electric field distributions on the plane $z = 1$ mm and $z = -0.635$ mm are different for M_3' and M_4' modes. From Fig. 4(d), it can be clearly observed that the input coupling line has constituted one pole of the hexapole mode and octopole mode for the M_3' and M_4' modes, indicating higher coupling efficiency between the input microstrip line and the corrugated MIM ring resonator. Thus less EM waves are reflected, more EM waves could be coupled out, and the insertion loss is decreased when l_f is 9 mm. Furthermore, the effective circumference length (including the input line) is increased and the resonance frequencies red shift. We can conclude that the increasing length of the input and output coupling lines affects the field distributions. Although the transmission band is broad, we can see that it's still not flat-top and the out-of-band rejection is not sharp.

Wideband filtering of spoof LSPs with flat-top transmission response and sharp out-of-band rejection. The lengths of the input and output coupling lines are further increased. The schematic configuration and the sample are shown in Fig. 4 and the filter is denoted as structure C. Figure 5(a) and (b) illustrate the top view and the bottom view of the proposed wideband bandpass filter, where the added stub length is denoted

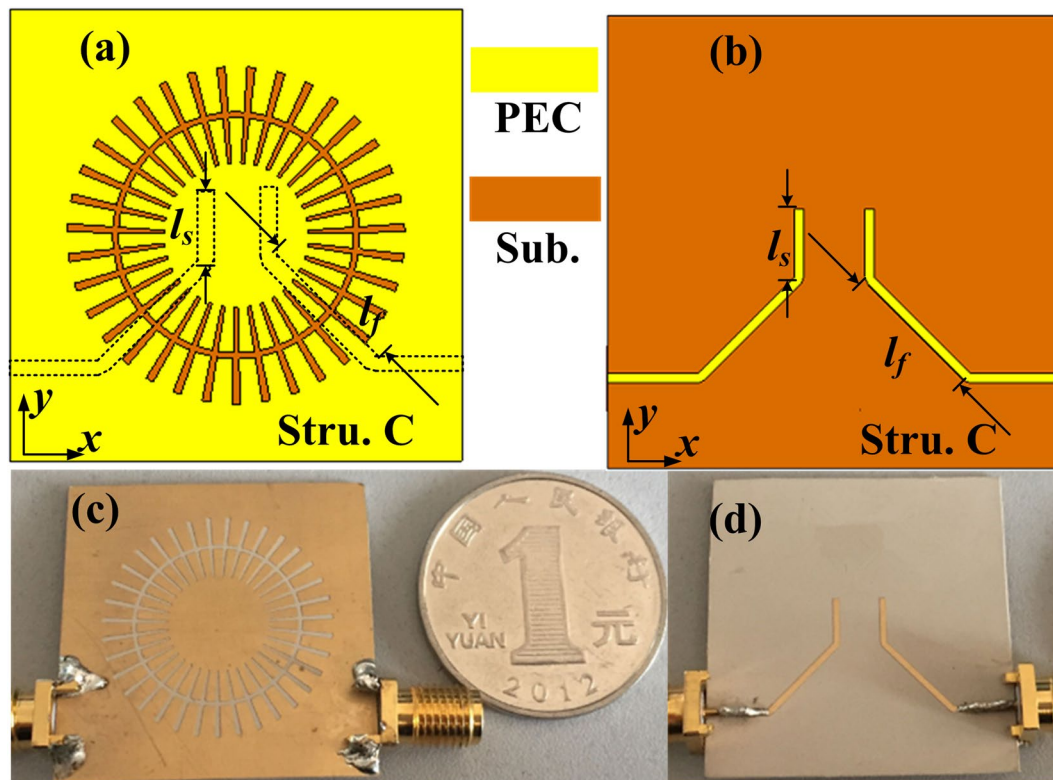


Figure 5. (a) The top view and (b) the bottom view of the schematic diagram of the wideband bandpass filter with flap-top transmission response (structure C). (c) The top view and (d) the bottom view of the fabricated wideband bandpass filter with flap-top transmission response.

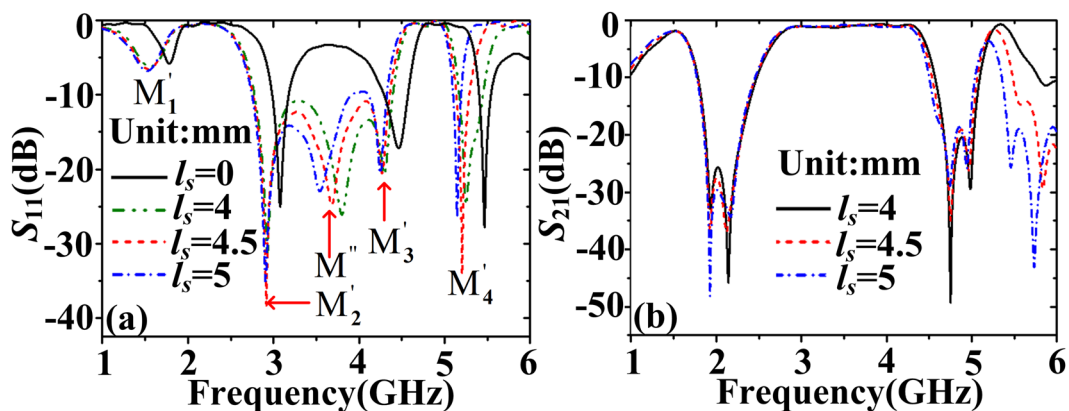


Figure 6. (a) Reflection coefficients and (b) transmission coefficients of the wideband bandpass filter with flap-top transmission response (structure C) when l_s changes.

as l_s . The fabricated sample is shown in Fig. 5(c) and (d), where the length l_f and l_s of the microstrip line are 9 mm and 4.5 mm, respectively.

The simulated reflection and transmission coefficients corresponding to different length l_s are given in Fig. 6(a) and (b). We can see that there are five resonance modes and their corresponding resonance frequencies are 1.54 GHz, 2.91 GHz, 3.70 GHz, 4.27 GHz, and 5.19 GHz when l_s is 4.5 mm. In addition to the normal resonance modes M_1' – M_4' , a new kind of resonance mode marked as M'' appears from Fig. 6(a). For the modes M_1' – M_4' , the resonance frequencies red shift compared with the case $l_s = 0$ from Fig. 6(a). With the increase of the length l_s (from 4 mm to 5 mm), the resonance frequencies of the modes M_1' – M_4' red shift, however, the changes are not obvious. While the redshift of the resonance frequency of the resonance mode M'' is obvious, indicating that this mode may be different from the modes M_1' – M_4' . From the results in Fig. 6(b), we can see that the transmission band has become flat-top due to the new mode M'' . The transmission band is from 2.65 GHz to 4.43 GHz and the insert loss is only -1 dB. The lower stopband (below -20 dB) is from 1.86 GHz to 2.30 GHz. The upper stopband

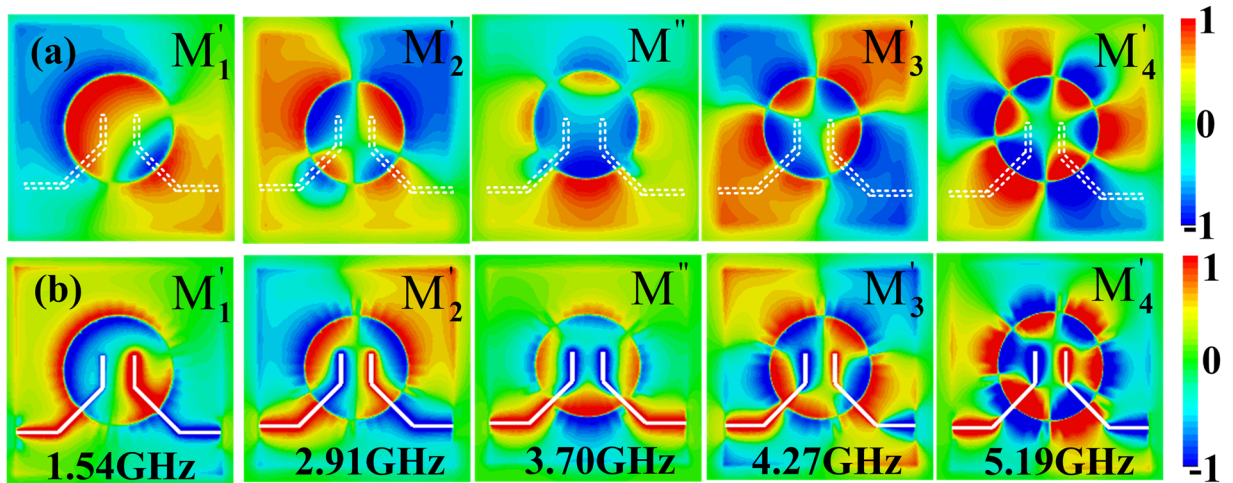


Figure 7. Simulated 2D E_z -field distributions (a) on the plane $z = 1$ mm and (b) on the plane $z = -0.635$ mm of the wideband bandpass filter with flap-top transmission response (structure C) when $l_s = 4.5$ mm and $l_f = 9$ mm.

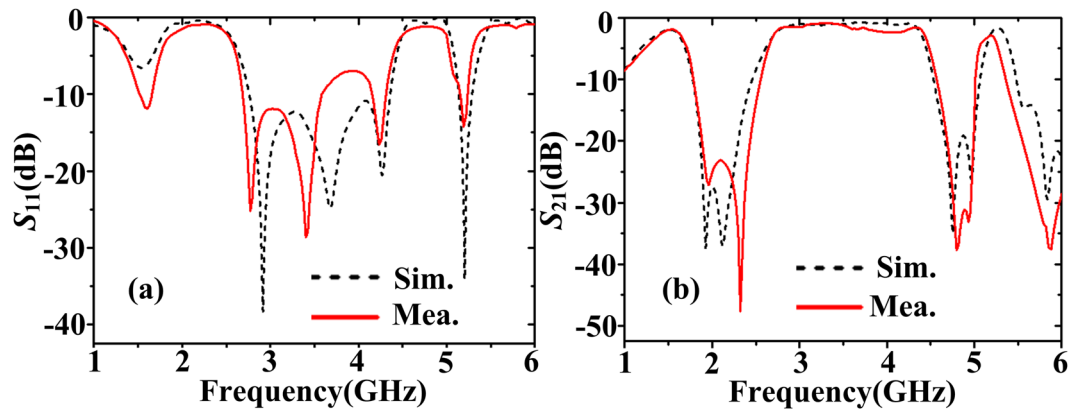


Figure 8. The simulated and measured (a) reflection coefficients and (b) transmission coefficients of the wideband bandpass filter with flap-top transmission response (structure C) when $l_s = 4.5$ mm and $l_f = 9$ mm.

is from 4.67 GHz to 5 GHz. Moreover, the out-of-band suppression is sharper. Especially, the whole structure is only $0.35\lambda * 0.35\lambda$, where λ is the wavelength at the center frequency in the passband.

To verify whether M'' is a new resonance mode, the 2D E_z -field distributions on the plane $z = 1$ mm and $z = -0.635$ mm at these resonant frequencies have been monitored and illustrated in Fig. 7(a) and (b). From Fig. 7(a), we can see that the M_1' and M_2' modes are dipole mode and quadrupole mode, while both M'' and M_3' mode are quadrupole mode and M_4' mode is hexapole mode. However, when we observe the 2D E_z -field distributions on the plane $z = -0.635$ mm illustrated in Fig. 7(b), it can be clearly seen that for M_2' , M_3' and M_4' modes, the input and output lines have actually become two poles of the quadrupole mode, hexapole mode, and octopole mode and the fields on the lines are out of phase. Different from these resonant modes, the fields for the resonance mode M'' are in phase. Hence, as the length l_s is increased, the effective inductance increases and the resonant frequency of the mode M'' red shifts obviously. Thus we can conclude that the mode M'' stems from the mutual inductive coupling of the input and output microstrip lines. While the modes $M_1' - M_4'$ are from the couplings between the input and output lines and the spoof plasmonic resonator. The changes of the resonance frequencies with the increase of l_s are small.

The measured reflection and transmission coefficients are plotted in Fig. 8(a) and (b). The measured resonance frequencies are 1.60 GHz, 2.77 GHz, 3.40 GHz, 4.24 GHz, and 5.19 GHz, respectively, which have good agreements with the simulated results. The slight resonance frequencies deviation could be caused by the dielectric constant difference between the simulation and the sample. The FWHM is from 2.67 GHz to 4.46 GHz and its relative bandwidth is 50.2%. Furthermore, the lower rejection band is from 1.87 GHz to 2.44 GHz. The transmission loss is a little larger than the simulation results at the higher frequencies, which may be due to the higher dielectric loss for the practical substrate. However, the out-of-band rejection in the measurement is sharper.

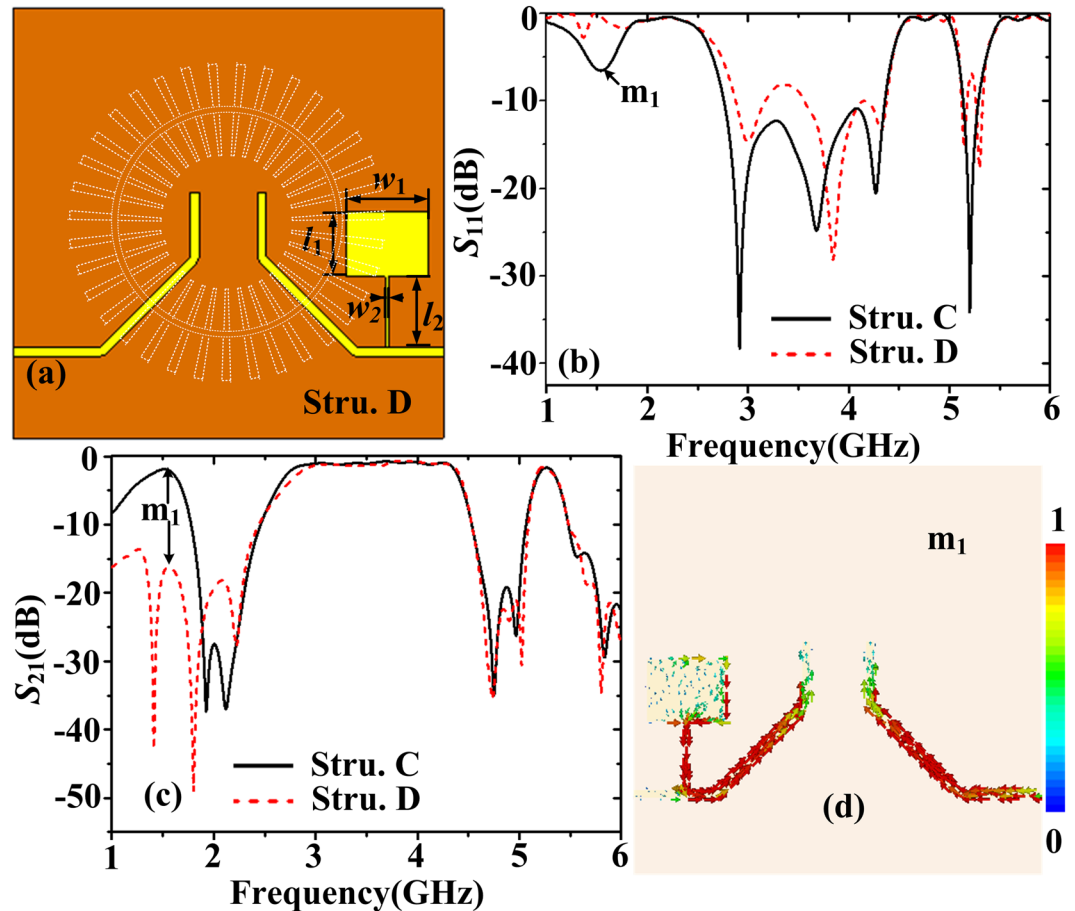


Figure 9. (a) The bottom view of the wideband bandpass plasmonic filter with a shunt SIR (structure D), where the parameters l_1 , l_2 , w_1 , and w_2 are 4.5 mm, 5 mm, 5.7 mm, and 0.2 mm, respectively. The simulated (b) reflection coefficients and (c) transmission coefficients of structure D. (d) Current distributions on the plane $z = -0.635$ mm of structure D at 1.57 GHz.

Rejection of out-of-band spoof LSPs modes. In consideration of practicality, all the frequencies outside the interested passband have to be rejected. First, a shunt SIR is added to the output microstrip line to acquire a new transmission zero³⁴, which consists of two impedance sections, as shown in Fig. 9(a). The filter is denoted as structure D. The lengths of the two impedance sections are l_1 and l_2 , and the widths are w_1 and w_2 , respectively. The designing principle is to make the SIR resonance frequency fall in the vicinity of the resonant frequency for the dipole mode. Hence the waves at the dipole mode would be coupled into the SIR structure and be rejected out of the interested passband. The parameters l_1 , l_2 , w_1 , and w_2 are optimized to 4.5 mm, 5 mm, 5.7 mm, and 0.2 mm, respectively. The reflection and transmission coefficients of the wideband filter with a shunt SIR are shown in Fig. 9(b) and (c). We can see that the dipole mode has been effectively suppressed. The current distributions on the plane $z = -0.635$ mm at 1.57 GHz (corresponding to the marked point m_1) have been illustrated in Fig. 9(d). As expected, it can be clearly seen that the dipole mode waves have been effectively coupled into the SIR structure.

Then to further reject the octopole ($n = 4$) mode, double C-shaped rings³⁵ are introduced on the back of the corrugated MIM ring, as illustrated in Fig. 10(a). The structure is called as structure E. The width, length, line width and gap width of the C-shaped ring are denoted as w_c , l_c , g_1 , and g_2 . The values of w_c , g_1 , and g_2 are set as 3 mm, 0.5 mm, and 0.5 mm, respectively. The distance g_r between the two C-shaped rings is 1 mm. It's known that the C-shaped ring can be efficiently excited by the transverse magnetic (TM) waves. The basic principle of rejecting the octopole mode is to make the resonant frequency of the double C-shaped rings fall in the vicinity of the resonant frequency for the octopole mode. To numerically calculate the resonant frequency of the double C-shaped rings using CST, the boundary conditions in y and z directions are set as the perfect electrical conductor (PEC) and perfect magnetic conductor (PMC) to support the TM waves, as shown in Fig. 10(b). The scattering parameters of the double C-shaped rings with the changing of l_c are shown in Fig. 10(c). Since the C-shaped ring can be represented by the parallel GLC model and the equivalent inductance L increases when l_c is increased, as expected the resonant frequencies red shift. Due to the strong coupling between the spoof LSPs resonator and the double C-shaped rings, it is expected that the octopole mode waves will be coupled into the double C-shaped rings and the mode can be rejected. The optimized l_c is 3 mm and the estimated resonant frequency is 5.57 GHz from Fig. 10(c). The transmission coefficients of the wideband filter with double C-shaped rings are shown in Fig. 10(d). It can be seen that the octopole mode has been suppressed with the transmission coefficients below

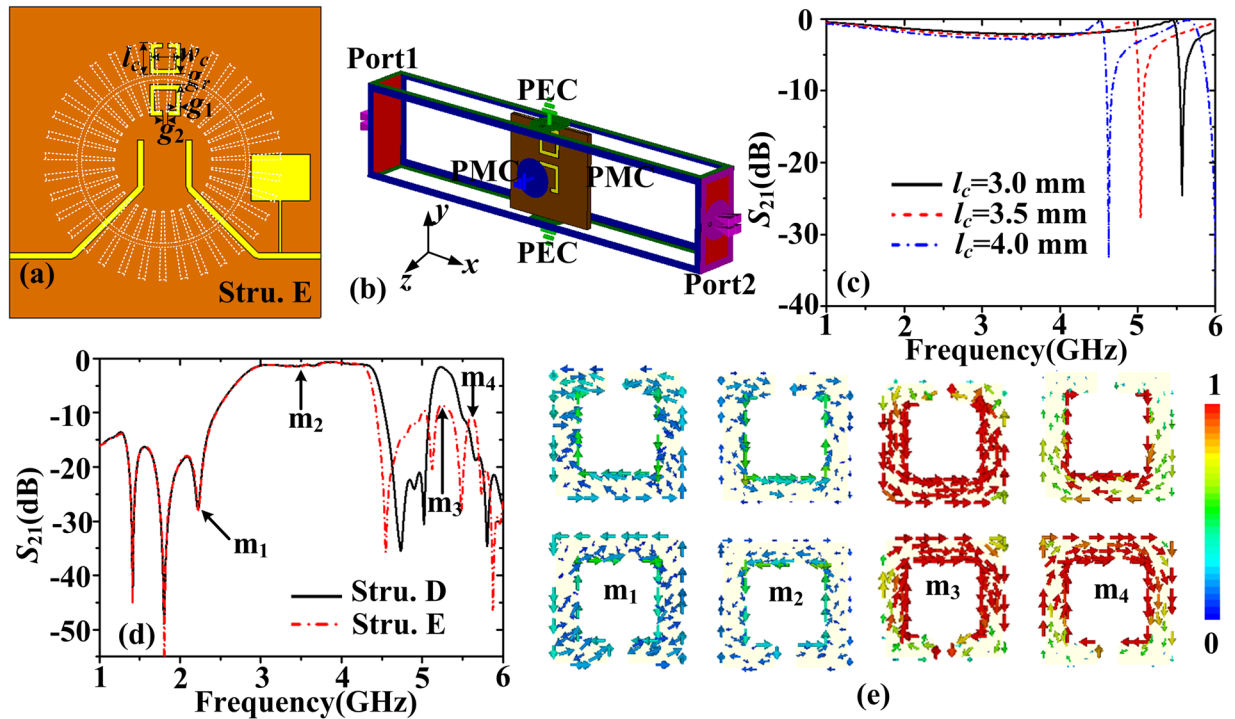


Figure 10. (a) The bottom view of the wideband plasmonic filter with a SIR and double C-shaped rings (structure E), where the values of w_c , g_1 , g_2 , and g_r are fixed to 3 mm, 0.5 mm, 0.5 mm, and 1 mm, respectively. l_c is optimized to 3 mm to make the octopole mode waves coupled into the double C-shaped rings. (b) The boundary conditions of the double C-shaped rings in the CST simulation. (c) The simulated transmission coefficients of the double C-shaped rings for different l_c . (d) The simulated transmission coefficients of structure E. (e) Current distributions on the plane $z = -0.635$ mm of structure E at 2.23 GHz, 3.5 GHz, 5.24 GHz and 5.62 GHz.

–10 dB. To confirm the coupling between the spoof LSPs resonator and the double C-shaped rings, the current distributions on the C-shaped rings at 2.23 GHz, 3.5 GHz, 5.24 GHz and 5.62 GHz, which are marked as m_1 – m_4 in Fig. 10(d), have been illustrated in Fig. 10(e). We can see that the magnitude of the current flow on the double C-shaped rings is small at m_1 – m_2 points, thus the coupling is weak. The current on the double C-shaped rings at m_3 and m_4 points are big and it indicates that the coupling is strong in the vicinity of the resonant frequency of the double C-shaped rings. Hence we can validate that it is the coupling between the double C-shaped rings and the spoof LSPs resonator which brings in the rejection of the octopole mode.

Discussion

Here we have theoretically and experimentally proposed an ultra-compact and wideband plasmonic filter based on corrugated MIM ring resonator. The proposed filter exhibits several attractive features such as compact size, wide bandwidth, low transmission loss, flat-top transmission response and sharp out-of-band suppression. Broad passband covering the quadrupole mode and the hexapole mode can be achieved by selecting proper lengths in the input and output coupling area. The mutual coupling between the input and output microstrip lines generates a new resonance mode and produces the flat-top transmission response and sharper out-of-band rejection. By introducing a shunt SIR and double C-shaped rings on the back of the substrate of the filter, the rejections of the dipole mode and the octopole mode can be achieved. The operating physical mechanism has been fully investigated, which can be expanded to THz frequencies. Simulated results agree well with the experimental results. The spoof plasmonic filter can find more applications in the highly integrated plasmonic circuits at microwave and THz frequencies.

Methods

Simulations and experiments. All samples are fabricated using Rogers RO3010 substrate whose relative dielectric constant is 10.2 and loss tangent is 0.0023. The numerical simulations are conducted with the help of the commercial software, CST Microwave Studio. The calculation of dispersion relations of the MIM ring resonator is based on CST eigenmode solver, where only one unit cell is analyzed and periodic boundary conditions (PBC) are used. The distributions of surface electric field and surface currents are calculated by use of CST transient solver, which is based on the finite-integral technique (FIT) method. Tetrahedral mesh and open boundary conditions are adopted. The fabricated sample is connected to Vector Network Analyzer (VNA, Agilent N5227A) to obtain the reflection and transmission coefficients.

References

1. Gramotnev, D. K. & Bozhevolnyi, S. I. Plasmonics beyond the diffraction limit. *Nat. Photonics* **4**, 83–91 (2010).
2. Kreibig, U. & Vollmer, M. Optical properties of metal clusters. *Springer* (1995).
3. Pendry, J. B., Martín-Moreno, L. & García-Vidal, F. J. Mimicking surface plasmons with structured surfaces. *Science* **305**, 847–848 (2004).
4. Williams, C. R. *et al.* Highly confined guiding of terahertz surface plasmon polaritons on structured metal surfaces. *Nat. Photonics* **2**, 175–179 (2008).
5. Gao, Z., Shen, L. F. & Zheng, X. D. Highly-confined guiding of terahertz waves along subwavelength grooves. *IEEE Photon. Technol. Lett.* **24**, 1343–1345 (2012).
6. Shen, X., Cui, T., Martín-Canon, D. & García-Vidal, F. J. Conformal surface plasmons propagating on ultrathin and flexible films. *Proc. Natl. Acad. Sci.* **110**, 40–45 (2013).
7. Pors, A., Moreno, E., Martín-Moreno, L., Pendry, J. B. & García-Vidal, F. J. Localized spoof plasmons arise while texturing closed surfaces. *Phys. Rev. Lett.* **108**, 223905 (2012).
8. Shen, X. & Cui, T. J. Ultrathin plasmonic metamaterial for spoof localized surface plasmons. *Laser Photonics Rev.* **8**, 137–145 (2014).
9. Gao, F. *et al.* Vertical transport of subwavelength localized surface electromagnetic modes. *Laser Photonics Rev.* **9**, 571–576 (2014).
10. Li, Z. *et al.* Localized spoof surface plasmons based on subwavelength closed high contrast gratings: concept and microwave-regime realizations. *Sci. Rep.* **6**, 27158 (2016).
11. Ma, H. F., Shen, X. P., Cheng, Q., Jiang, W. X. & Cui, T. J. Broadband and high-efficiency conversion from guided waves to spoof surface plasmon polaritons. *Laser Photonics Rev.* **8**, 146–151 (2014).
12. Ye, L. F. *et al.* Plasmonic waveguide with folded stubs for highly confined terahertz propagation and concentration. *Opt. Express* **25**, 898–906 (2017).
13. Kianinejad, A., Chen, Z. N. & Qiu, C. W. Low-loss spoof surface plasmon slow-wave transmission lines with compact transition and high isolation. *IEEE Trans. Microwave Theory Tech.* **64**, 3078–3086 (2016).
14. Zhao, L. *et al.* A novel broadband band-pass filter based on spoof surface plasmon polaritons. *Sci. Rep.* **6**, 36069 (2016).
15. Xu, J. *et al.* Low-pass plasmonic filter and its miniaturization based on spoof surface plasmon polaritons. *Opt. Commun.* **372**, 155–159 (2016).
16. Neutens, P., Van Dorpe, P., De Vlamincq, I., Lagae, L. & Borghs, G. Electrical detection of confined gap plasmons in metal-insulator-metal waveguides. *Nat. Photonics* **3**, 283–286 (2009).
17. Kats, M. A., Woolf, D., Blancha, R., Yu, N. & Capasso, F. Spoof plasmon analogue of metal-insulator-metal waveguides. *Opt. Express* **19**, 14860–14870 (2011).
18. Gao, X., Zhou, L., Liao, Z., Ma, H. F. & Cui, T. J. An ultra-wideband surface plasmonic filter in microwave frequency. *Appl. Phys. Lett.* **104**, 191603 (2014).
19. Zhou, Y. J. & Yang, B. J. Planar spoof plasmonic ultra-wideband filter based on low-loss and compact terahertz waveguide corrugated with dumbbell grooves. *Appl. Opt.* **54**, 4529–4533 (2015).
20. Hu, M. Z. *et al.* Ultra-wideband filtering of spoof surface plasmon polaritons using deep subwavelength planar structures. *Sci. Rep.* **6**, 37605 (2016).
21. Tao, J., Huang, X. G., Lin, X., Zhang, Q. & Jin, X. P. A narrow-band subwavelength plasmonic waveguide filter with asymmetrical multiple-teeth-shaped structure. *Opt. Express* **17**, 13989–13994 (2009).
22. Zhan, G. Z., Liang, R. S., Liang, H. T., Luo, J. & Zhao, R. T. Asymmetric band-pass plasmonic nanodisk filter with mode inhibition and spectrally splitting capabilities. *Opt. Express* **22**, 9912–9919 (2014).
23. Yang, B. J., Zhou, Y. J. & Xiao, Q. X. Spoof localized surface plasmons in corrugated ring structures excited by microstrip line. *Opt. Express* **23**, 21434–21442 (2015).
24. Liao, Z. *et al.* Combined system for efficient excitation and capture of LSP resonances and flexible control of SPP transmissions. *ACS Photonics* **2**, 738–743 (2015).
25. Xu, B. Z. *et al.* Tunable band-notched coplanar waveguide based on localized spoof surface plasmons. *Opt. Lett.* **40**, 4683–4686 (2015).
26. Wang, H. Q. *et al.* Tunable band-stop plasmonic waveguide filter with symmetrical multiple-teeth-shaped structure. *Opt. Lett.* **41**, 1233–1236 (2016).
27. Chen, Z. Q. *et al.* Tunable ultra-wide band-stop filter based on single-stub plasmonic-waveguide system. *Appl. Phys. Express* **9**, 102002 (2016).
28. Gao, Z., Gao, F., Shastri, K. K. & Zhang, B. L. Frequency-selective propagation of localized spoof surface plasmons in a graded plasmonic resonator chain. *Sci. Rep.* **6**, 25576 (2016).
29. Li, Z. *et al.* Coplanar waveguide wideband band-stop filter based on localized spoof surface plasmons. *Appl. Opt.* **55**, 10323–10328 (2016).
30. Sun, S. & Zhu, L. Wideband microstrip ring resonator bandpass filters under multiple resonances. *IEEE Trans. Microwave theory tech.* **55**, 2176–2182 (2007).
31. Chen, C. H. Plasmonic bandpass filters with cascaded rectangular ring resonators. *Opt. Lett.* **39**, 3227–3230 (2014).
32. Zhou, Y. J., Xiao, Q. X. & Yang, B. J. Spoof localized surface plasmons on ultrathin textured MIM ring resonator with enhanced resonances. *Sci. Rep.* **5**, 14819 (2015).
33. Cohn, S. B. Slotline on a dielectric substrate. *IEEE Trans. Microw. Theory Tech.* **17**, 768–778 (1969).
34. Zhang, S. & Zhu, L. Synthesis design of dual-band bandpass filters with lambda/4 stepped-Impedance resonators. *IEEE Trans. Microwave theory tech.* **61**, 1812–1819 (2013).
35. Zhou, Y. J. & Xiao, Q. X. Electronically controlled rejections of spoof surface plasmons polaritons. *J. Appl. Phys.* **121**, 123109 (2017).

Acknowledgements

This work was supported in part by Natural Science Foundation of China under Grant No. 61307129, in part by STCSM under Grant No. SKLSFO2017-05, and in part by the Shanghai Committee of Science and Technology under Grant No. 13ZR1454500.

Author Contributions

L.Y. and Y.J.Z. conceived the idea. L.Y. conducted the numerical simulations. L.Y., C.Z. and Q.X.X. performed the experimental measurements. Y.J.Z. and L.Y. wrote the manuscript.

Additional Information

Competing Interests: The authors declare that they have no competing interests.

Publisher's note: Springer Nature remains neutral with regard to jurisdictional claims in published maps and institutional affiliations.



Open Access This article is licensed under a Creative Commons Attribution 4.0 International License, which permits use, sharing, adaptation, distribution and reproduction in any medium or format, as long as you give appropriate credit to the original author(s) and the source, provide a link to the Creative Commons license, and indicate if changes were made. The images or other third party material in this article are included in the article's Creative Commons license, unless indicated otherwise in a credit line to the material. If material is not included in the article's Creative Commons license and your intended use is not permitted by statutory regulation or exceeds the permitted use, you will need to obtain permission directly from the copyright holder. To view a copy of this license, visit <http://creativecommons.org/licenses/by/4.0/>.

© The Author(s) 2017